Constraints on the Lateral Variations of the Martian Crustal Thickness from Seismological and Gravity Field Measurements

Mélanie Drilleau[1], Henri Samuel[2], Raphaël F. Garcia[1], Attilio Rivoldini[3], Clément Perrin[4], Mark Wieczorek[2], Philippe Lognonné[2], William B. Banerdt[5]

[1]Institut Supérieur de l'Aéronautique et de l'Espace ISAE-SUPAERO, 10 Avenue Edouard Belin, 31400 Toulouse, France
[2]Université Paris Cité, Institut de physique du globe de Paris, CNRS, Paris, France
[3]Royal Observatory of Belgium, Brussels, Belgium
[4]Nantes Université, Université d'Angers, Le Mans Université, CNRS, UMR 6112, Laboratoire de Planétologie et Géosciences, UAR 3281, Observatoire des Sciences de l'Univers de Nantes Atlantique, Nantes, France
[5]Jet Propulsion Laboratory, California Institute of Technology

S. 1 Seismic travel time data set

The body waves arrival times database used in this study is shown in Table S1.1.

S. 2 Geodynamical parameters

This section provides a summary of the inversion output and information on the geodynamic interpretation of the output models from the inversion sets. Further details on the geodynamical parameterization can be found in Drilleau et al. (2021, 2022).

S. 2.1 Summary of the inverted geodynamical quantities

The list of inverted parameters and the corresponding prior bounds considered, is summarized in Table S2.1. The mean output values of a selection of geodynamical quantities, and their 1-σ standard deviations, are summarized in Table S2.2. The input parameters of the Bayesian algorithm are indicated with the superscript '$\star$'. The other parameters are derived from the input parameters and the geodynamical modeling.

S. 2.2 Approximate expression for the lithospheric temperature gradient

The lithospheric temperature gradient in the output models can be estimated as:

$$\frac{dT_l}{dz} = \frac{T_l - T_{\mathrm{cr}}}{D_l}, \tag{S2.1}$$

where z is the depth from the surface, T_{cr} is the temperature at the base of the crust, T_l is the temperature at the base of the lithosphere, and D_l is the thickness of the lithosphere (excluding the crustal thickness D_{cr} and the uppermost mantle thermal boundary layer). One can estimate T_{cr} with the knowledge of the surface heat flux F_s and the crustal thickness at the present-day:

$$F_s \cong -k_{\mathrm{cr}} \frac{T_s - T_{\mathrm{cr}}}{D_{\mathrm{cr}}}, \tag{S2.2}$$

where T_s=220 K is the surface temperature, and $k_{\mathrm{cr}} = 2.5$ W m^{-1}K^{-1} is the crustal thermal conductivity. For all models F_s lies within similar ranges: 20–23 mW m^{-2}. This results from the fact that the same bulk content in heat-producing elements is used for all models, which eventually controls the present-day heat loss at the surface (Drilleau et al., 2021). Similarly, D_{cr} for all models have comparable values: $D_{\mathrm{cr}} \cong 66$ km (Table S2.2). This leads to $T_{\mathrm{cr}} \cong 780$ K.

Following Samuel et al. (2019) the temperature at the base of the lithosphere is:

$$T_l = T_m - a_{\mathrm{rh}} \frac{R\, T_m^2}{E^*}, \tag{S2.3}$$

where $a_{\mathrm{rh}} = 2.54$ (Thiriet et al., 2018) and $R = 8.3$ J mol^{-1}K^{-1}, hence:

$$T_l \cong T_m \left(1 - 20\, T_m/E^*\right). \tag{S2.4}$$

Combining Equations (S2.1) and (S2.4) yields the following expression for the lithospheric temperature gradient:

$$\frac{dT_l}{dz} = \frac{T_m \left(1 - 20\, T_m/E^*\right) - 780}{D_l}. \tag{S2.5}$$

Table S1.1. Summary of back azimuth measurements and observed body wave differential travel times (in seconds). The epicentral distances constrained by the 1D inversion are also indicated. When the differential time cannot be estimated, a "-" marker is indicated. Error bars for direct P- and S- phases arrival times are 5 s. Error bars for PP and SS are 8 s and 5 s, respectively. Error bars for PPP and SSS are 12 s and 8 s, respectively. Concerning the depth phases, the error bars are equal to 3 s for pP arrival times, and 5 s for sP and sS arrival times. Error bars for ScS phases are 12 s. Error bars for SS-PP and SKS-PP are considered to be 10 s. The superscripts '⋆' indicate the impact events.

Event	Back azimuth (°)	Epicentral distance (°)	S-P (s)	pP-P (s)	sP-P (s)	PP-P (s)	PPP-P (s)	sS-S (s)	SS-S (s)	SSS-S (s)	ScS-S (s)	SS-PP (s)	SKS-PP (s)
S0154a	87±55.6	29.9±2.2	174.4	-	-	-	-	-	25.3	35	-	-	-
S0173a	91±17.6	30.2±1.5	178.8	-	9.43	19.9	34.4	13.2	24.4	40.5	345.2	-	-
S0185a	319±13.7	54.7±1.6	327.28	4	-	22.47	49.3	10	30.9	55.4	152.3	-	-
S0235b	69±14.6	29.2±1.5	171.4	-	-	18.6	32	9.2	23.2	33.3	343.9	-	-
S0325a	125.5±17.0	41.5±2.0	229.3	9.8	-	21.1	34.4	13.8	26.1	50.3	220.4	-	-
S0407a	79±24.5	27.9±1.6	170.7	6.77	-	23.38	-	13.3	21.1	33.1	370	-	-
S0409d	82±25.0	30.3±2.2	163.2	8.3	-	27.6	36.94	8.4	20.9	39.8	320.1	-	-
S0474a	21±48.8	19.7±2.5	121.6	-	-	13.4	24.8	-	15.8	32.4	-	-	-
S0484b	73±33.7	30.9±1.4	173.1	5.5	-	19.73	-	13	17.4	-	322.3	-	-
S0784a	100.5±17.0	30.6±1.9	179.3	6.5	-	13.7	22.4	7.2	19.6	28	-	-	-
S0802a	85±19.5	27.9±2.3	180.3	4	-	25.6	33.9	9.3	22.4	36.5	387.6	-	-
S0809a	86.3±15.2	29.4±2.8	191.95	4.5	-	16.25	29.65	8.1	23.8	39.3	373.5	-	-
S0820a	84±17.9	29.4±2.3	174.1	-	-	21.9	32.1	8.5	-	-	-	-	-
S0861a	313±15.0	55.1±3.0	319.3	-	-	19.6	47.6	-	41.1	-	-	-	-
S0864a	83.5±34.5	29.5±3.3	171.4	-	-	18	27.9	17.3	26.4	-	-	-	-
S0916d	71±25.3	29.4±1.4	170.8	3.9	-	19.3	36.1	-	19	42.9	342.8	-	-
S0918a	161.5±28.9	16.8±2.2	102.4	-	-	12.8	22.5	-	21.2	35	-	-	-
S0976a	81.5±18.4	143.6±2.6	-	-	-	-	-	-	-	-	-	854.4	303.9
S1000a⋆	34.0	126.09	-	-	-	-	-	-	-	-	-	749.0	339.3
S1012d	62.5±14.0	37.6±1.9	221.7	6.7	-	18	27.7	11	24.5	40.65	-	-	-
S1015f	80.5±21.8	30.1±2.1	177.7	-	-	20.47	35.37	11.2	-	-	-	-	-
S1022a	88.5±18.5	29.4±2.2	177	9	-	19.3	27.5	11	25	55	-	-	-
S1039b	140±21.8	30.1±2.8	176.1	7.8	-	12.3	28.7	-	14.9	-	-	-	-
S1048d	74±21.8	30.8±1.7	179.19	7.49	-	18.05	-	-	24.3	-	-	-	-
S1094b⋆	51.4	58.5	343.0	-	-	-	-	-	-	-	-	-	-
S1102a	81±21.8	75.7±2.9	443.7	-	-	-	-	-	-	-	-	-	-
S1133c	88±21.8	29.5±2.1	175.3	5.8	-	16.7	28.46	9.1	17.4	35.4	-	-	-
S1153a	97±20.0	82.2±2.7	467.95	-	-	-	-	-	-	-	-	-	-
S1157a	87.5±20.8	36.9±2.1	215.8	-	-	18.7	-	14.6	39.6	-	-	-	-
S1197a	243±66.0	32.2±2.0	191.2	8.4	-	15.4	-	14.7	-	-	-	-	-
S1222a	124±18.4	37.6±2.4	216.0	-	-	28.0	37.8	-	-	-	258	-	-

Table S2.1. List of parameters inverted in the McMC algorithm, and the corresponding prior bounds considered. The subscripts '0' indicate initial values for quantities that vary in time.

Inverted parameter	Meaning	Range	Units
E^*	Mantle effective activation energy	100 - 500	kJ/mol
V^*	Mantle effective activation volume	0 - 10	cm^3/mol
η_0	Mantle reference viscosity	10^{20} - 10^{23}	Pa s
T_{m_0}	Initial uppermost mantle temperature	1700 - 2000	K
T_{c_0}	Initial CMB temperature	$T_{c_0} - T_{m_0} = 300 - 600$	-
Λ	HPE crustal enrichment	5-20	-
R_c	Core radius	1400 - 2000	km
K_S	Core isentropic bulk modulus at CMB	120 - 200	GPa
K'_S	Pressure derivative of K_S	2-7	-
V_{S_1}	V_S in the upper crust (layer 1)	1.0 - 3.0	km/s
V_{S_2}	V_S in the mid-crust (layer 2)	2.0 - 3.5	km/s
V_{S_3}	V_S in the lower crust (layer 3)	3.9 - 4.4	km/s
V_P/V_S	V_P/V_S in the entire crust	1.7 - 1.9	-
Δ	Source epicentral distance	0 - 180 (except for S1000a and S1094b)	°
$pDepth$	Source depth	5 - 200 (except for S1000a and S1094b)	km

Table S2.2. Summary of the inversion results. Quantities listed correspond to constant or to present-day mean values and 1-σ uncertainty unless specified otherwise. The superscripts '$\star$' indicate the input parameters of our geodynamical model, that we vary in the inversion algorithm (top). The other parameters are derived from the input parameters and the geodynamical modeling (bottom). The subscripts '0' indicate initial values for quantities that vary in time.

Inverted parameter	Meaning	1D	Family A (3D)	Family B (3D)	Units
E^*	Mantle effective activation energy *	318 ± 98	259 ± 107	135 ± 19	kJ/mol
V^*	Mantle effective activation volume *	5.3 ± 2.4	5.6 ± 2.1	7.2 ± 2.3	cm^3/mol
η_0	Mantle reference viscosity *	$10^{21.7\pm0.5}$	$10^{22\pm0.4}$	$10^{20.5\pm0.3}$	Pa s
T_{m_0}	Initial uppermost mantle temperature *	1758 ± 39	1748 ± 31	1830 ± 64	K
T_{c_0}	Initial CMB temperature *	2197 ± 70	2182 ± 77	2279 ± 79	K
Λ	HPE crustal enrichment *	10.1 ± 0.6	10.3 ± 0.5	9.3 ± 1.1	-
R_c	Core radius *	1839 ± 25	1832 ± 23	1796 ± 33	km
K_S	Core isentropic bulk modulus at CMB *	144 ± 10	145 ± 11	145 ± 12	GPa
K_S'	Pressure derivative of K_S *	4.2 ± 1.2	4.1 ± 1.2	4.4 ± 1.1	-

Output parameter	Meaning	1D	Family A (3D)	Family B (3D)	Units
T_p	Potential temperature	1770 ± 69	1824 ± 63	1466 ± 31	K
T_m	Uppermost mantle temperature	1831 ± 77	1886 ± 70	1493 ± 34	K
T_c	CMB temperature	2047 ± 63	2096 ± 50	1899 ± 86	K
D_{cr}	Crustal thickness	$68.7^{+2.0}_{-3.2}$	$64.2^{+3.6}_{-3.9}$	$63.6^{+4.0}_{-6.1}$	km
$D_{cr_{InSight}}$	Crustal thickness at the InSight landing site	$68.7^{+2.0}_{-3.2}$	$44.9^{+1.3}_{-2.6}$	$44.6^{+1.5}_{-3.4}$	km
D_{lu}	Lithospheric and upper thermal boundary layer thickness	583 ± 79	630 ± 111	426 ± 96	km
ρ_{cr}	Crustal density	unconstrained	3014^{+62}_{-133}	2992^{+79}_{-214}	kg/m^3
$\Delta\rho_{m-cr}$	$\rho_m - \rho_{cr}$ at Moho	656 ± 175	447^{+133}_{-63}	466^{+207}_{-79}	kg/m^3
ρ_{CMB}	Core density at CMB	5724 ± 107	5672 ± 73	5642 ± 104	kg/m^3
ρ_c	Average core density	5971 ± 111	5908 ± 74	5864 ± 102	kg/m^3
F_s	Surface heat flux	21.1 ± 0.5	20.8 ± 0.6	21.0 ± 1.0	mW/m^2
dT_l/dr	Lithospheric thermal gradient	1.88 ± 0.12	1.97 ± 0.13	1.74 ± 0.18	K/km

S. 2.3 Origin of Families A and B

As discussed in the main text, the 3D inversion set has revealed the existence of two distinct families A and B within the population of output models, as seen in panels (a2-f2) and (a3-f3) of Figure 2 and in Table S2.2. The clear distinction between these two subsets of models results from the combination between the geodynamical quantities inverted for. In particular, the mantle rheology, the crustal enrichment relative to the primitive mantle (Λ), and the initial thermal state. Several combinations of these quantities lead to extensive shallow mantle melting early on, resulting in thick crusts. This results in model rejection for two possible reasons:

1. Models where the present-day crustal thickness is larger than the maximum allowed bound of 72 km (see main text).
2. Models whose crustal growth combined with relatively large crustal enrichment values entirely depletes the underlying mantle in HPEs. Indeed, the HPE concentration in the mantle in the parameterized thermal evolution model used in the inversion scheme is described by the following mass balance equation (Breuer & Spohn, 2003; Grott & Breuer, 2008; Thiriet et al., 2018; Samuel et al., 2019):

$$H_m = \sum_i H_{0,i} \exp(-\lambda_i t) \left(1 + \frac{V_{cr}}{V_m}(1 - \Lambda) \right) \qquad (S2.6)$$

where $H_{0,i}$ is the individual contribution of heat-producing elements (^{238}U, ^{235}U, ^{232}Th, ^{40}K) at initial time $t = 0$, λ_i are the corresponding radioactive decay constants V_m is the volume of the mantle (including the lithosphere), and V_{cr} is the volume of the crust. The above mass balance shows that beyond the point where $\Lambda > 1 + V_m/V_{cr}$ any further growth of the crust (or V_{cr}) would then result in non-physical negative HPE concentrations in the mantle to satisfy mass balance considerations.

While the first condition leading to model rejection cannot be avoided, the second condition above could be relaxed to some extent by considering a crustal enrichment based on partition coefficients HPEs as done in (Morschhauser et al., 2011; Hauck & Phillips, 2002; Tosi et al., 2017). In this case, models falling into this category would not be rejected but would be associated with smaller crustal enrichment values. Therefore, overall one would still expect the appearance of two distinct families. This will be investigated in the future in greater detail.

Note that even though the present-day crustal thickness is an output parameter of our inversion, we do not directly sample its value, contrary to other parameters we invert for (*i.e.*, the mantle viscosity or initial thermal state, see Table S2.1). This is because in the frame of our geodynamical parameterization, the crustal thickness for each model evolves for 4.5 Gyr depending on the thermal evolution of the mantle. Following Morschhauser et al. (2011) and Samuel et al. (2019), the crust grows via melt extraction at shallow depth. More specifically, the crustal growth rate dD_{cr}/dt is proportional to the amount of shallow mantle melting produced, $m_a(t)$, and to the magnitude of convective velocities $v_{\text{conv}}(t)$ (see Equation (17) in Samuel et al. (2019) and references therein). The former is directly proportional to the thermal state of the mantle $m_a \propto T_m(t)$, and the latter is proportional to the time-dependent Rayleigh number (which expresses the mantle convective vigor) raised to a power, $v_{\text{conv}} \propto Ra(t)^{2/3}$. The Rayleigh number itself is a function of mantle rheology, core size, and evolving thermal state. Therefore, in addition to the HPE mass balance requirement mentioned above, this complex time-dependent combination of influences implies that we do not have a direct control on this parameter, unlike the mantle rheology, the core size or the initial thermal state, which we can directly sample.

For this reason, the prior for the present-day crustal thickness can significantly deviate from a Gaussian distribution. This is illustrated in Figure S2.1 which shows the correlation between the present-day crustal thickness D_{cr} and the mantle potential temperature T_p obtained by sampling the prior distribution without the crustal constraints of Wieczorek et al. (2022). When no constraints on the crustal thickness are applied, one can see a correlation between D_{cr} and T_p, with generally colder thermal states being associated with thinner crusts. In this phase space, one can distinguish two main patches that are, however, not completely disconnected. Applying the constraints from Wieczorek et al. (2022) on the crustal thickness restricts the phase space (below the red dashed line in Figure S2.1) thereby resulting in different D_{cr} and T_p correlations, where bimodality is enhanced. This correlation results in a bimodal prior distribution displayed in Figure S2.2 for the inversion set without constraints (panel a) or with constraints on the present-day crustal thickness (panel b). The bimodal character of T_p is weak but distinguishable when no crustal thickness constraints are applied, but strongly enhanced when crustal constraints are considered.

The posterior distributions of the average present-day crustal thickness and of the crustal thickness below each epicenter locations (in the case of 3D models), are provided in Sections S. 6 and S. 9 for cases with and without the crustal constraints of Wieczorek et al. (2022), respectively.
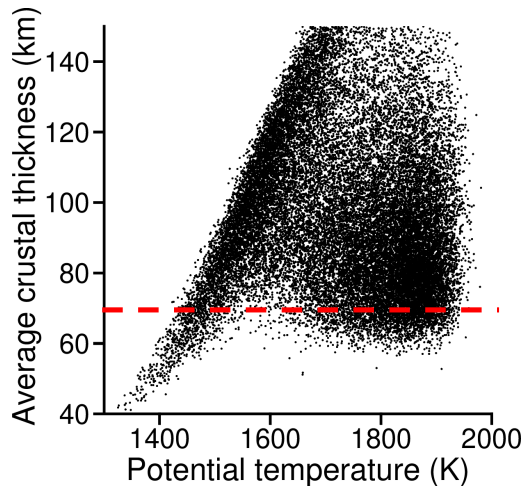
Figure S2.1. Prior distribution of the potential temperature as a function of the average crustal thickness. The models are randomly sampled within the prior bounds, without the constraints of Wieczorek et al. (2022) on the crustal thickness. The red dashed line delimits the upper bound at 72 km of Wieczorek et al. (2022).
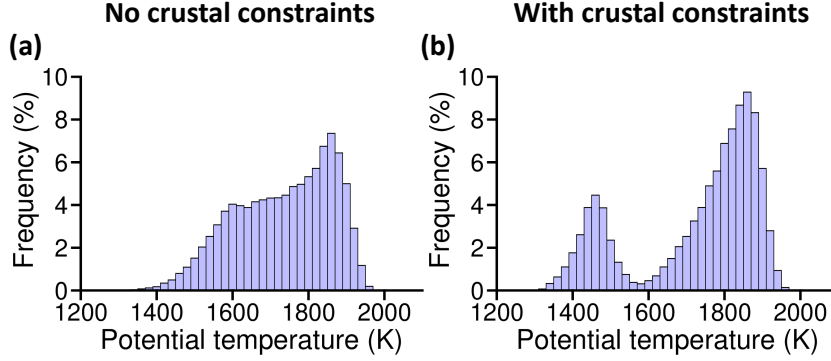
No crustal constraints   **With crustal constraints**

Figure S2.2. Marginal prior distributions of the potential temperature, without (a) or with (b) constraints of Wieczorek et al. (2022) on the crustal thickness.

S. 3 Inverse problem and data fit

Due to the ill-posed nature of the problem, we use a Bayesian approach to solve the inverse problem (*e.g.*, Mosegaard & Tarantola, 1995; Tarantola, 2005). Let us denote by the vectors $\mathbf{p}$ and $\mathbf{d}$, the parameters of our model and the observed data, respectively. $\mathbf{d}$ are related to $\mathbf{p}$ through the equation $\mathbf{d} = A(\mathbf{p})$, where the non-analytic and nonlinear operator A represents the forward problem discussed in Section 2 (main text). In this study the data $\mathbf{d}$ are the differential arrival times of body waves detailed in Table S1.1, and the degree-two Love number (k_2) estimate from Konopliv et al. (2020). The parameters $\mathbf{p}$ are described in Table S2.1. In this framework, the solutions of the inverse problem are described by the posterior probability distributions $P(\mathbf{p} \mid \mathbf{d})$ that the parameters are in a configuration $\mathbf{p}$ given the data are in a configuration $\mathbf{d}$. The prior distribution $P(\mathbf{p})$, which represents our current state of knowledge, is linked to the posterior distribution $P(\mathbf{p} \mid \mathbf{d})$ through the Bayes' theorem:

$$P(\mathbf{p} \mid \mathbf{d}) = \frac{P(\mathbf{d} \mid \mathbf{p})P(\mathbf{p})}{\sum_{\mathbf{p}\in\mathcal{M}} P(\mathbf{d} \mid \mathbf{p})P(\mathbf{p})}, \tag{S3.1}$$

where $\mathcal{M}$ denotes all the configurations in the parameter space. The posterior distribution $P(\mathbf{p} \mid \mathbf{d})$ is a function of the misfit $\mathcal{S}$, which is a measure of the similarity between observed data and the predictions.

Following the previous studies of *e.g.* Drilleau et al. (2022); Durán et al. (2022); Irving et al. (2023); Samuel et al. (2023); Stähler et al. (2021), we assume that the data noise is uncorrelated and described by a Laplacian distribution (L_1 norm), which is less prone to be affected by outliers than the Gaussian distribution (L_2 norm) (*e.g.*, Tarantola, 2005). The misfit function is thus evaluated as follows:

$$\mathcal{S} = \sum_{i}^{N} \frac{\mid t_i^{obs} - t_i^{cal} \mid}{\sigma_{t_i}} + \frac{\mid k_2^{obs} - k_2^{cal} \mid}{\sigma_{k_2}}, \tag{S3.2}$$

where superscripts throughout refer to observations (obs) and computed data (calc). For body waves, since the origin time of the seismic events remains unknown, we use differential times relative to the P- and S-waves phase arrivals (Table S1.1). t_i^{obs} and σ_{t_i} thus denotes the i-th differential times and its uncertainty, with N expressing the total number of observed differential travel times ($N = 161$) detailed in Table S1.1. For k_2, we use the observations of Konopliv et al. (2020): $k_2 = 0.174 \pm 0.016$.

To infer the posterior distribution of the parameters (Equation S3.1), we use the Metropolis algorithm (Metropolis et al., 1953). This algorithm samples the model space

in a random fashion, ensuring that low probability areas are sampled less extensively, with a sampling density proportional to the unknown (target) posterior pdf. The Metropolis algorithm relies on a randomized decision rule, which accepts or rejects the proposed model according to its fit to the data, and if the model satisfies the prior conditions.

The data fit on the differential arrival times is shown in Figure S3.1. The observed data (Table S1.1) are represented with symbols, and the calculated data with a probability density function (pdf). We can argue that the majority of models, considering a 1D or a 3D crust, fit the data within uncertainty bounds, which means that almost all the sampled models are able to explain the seismic data. However, for Family B, the fit of $t_{SS} - t_{PP}$ for the S0976a event is not as good as the ones of 1D models and Family A (Figure S3.1d-f). This is reflected in the larger uncertainty about the location of the S0976a event (Tables S7.1 and S7.2), because this event is located along the crustal dichotomy boundary. The 1D models and Family A fit the k_2 data of Konopliv et al. (2020) within 2σ uncertainty (Figure S3.2a,b). However, the k_2 values of Family B are smaller (Figure S3.2c) and 33 % of the models shows a $k2$ value smaller than the -2σ of Konopliv et al. (2020) because of their smaller core radii and stiffer mantles. Distributions of the total cost function $\mathcal{S}$ (Equation S3.2) are shown in Figure S3.3.

S. 4 Output seismic models

Figure S4.1 represents the *a posteriori* probability density functions (pdfs) of V_S and V_P, for the 1D and 3D models. The pdfs provide an overview of the most frequently sampled models, but this representation has a tendency to smooth the results. Compared to 1D models (Figure S4.1a,c), a bimodal distribution is clearly observed when a 3D crust is considered (Figure S4.1b,d), with three quarters belonging to Family A and one quarter to Family B. The models of these two families of the bimodal distribution (Figure S4.1b,d) are represented separately in Figure 1b,c of the main text, as Families A and B. The *a posteriori* pdfs of V_S and V_P for each family (1D, Family A, Family B) are shown in Figure S4.2.
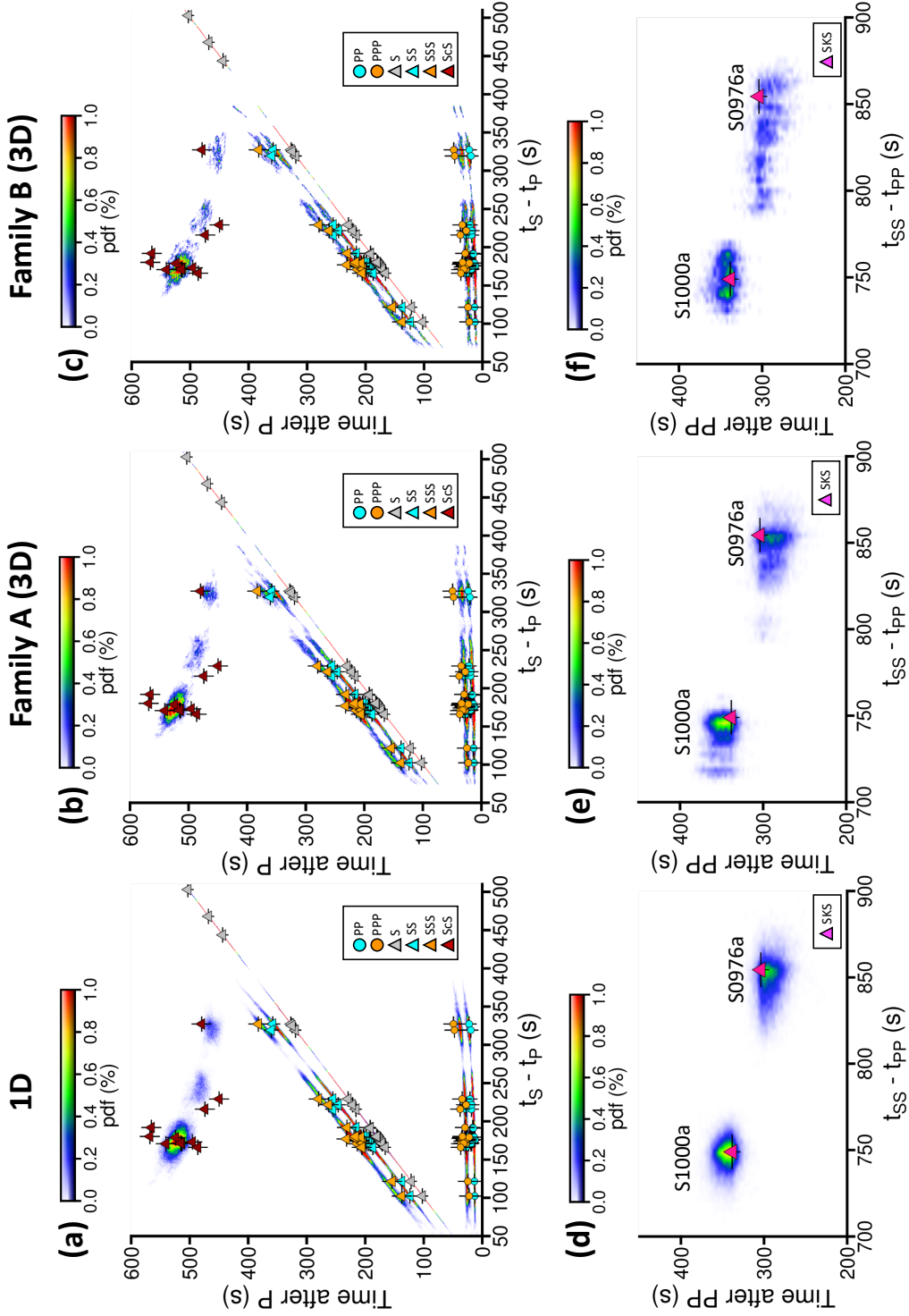
Figure S3.1. Fit of data for the differential arrival times, considering 1D models (left) and 3D Families A (middle) and B (right). The results are displayed in terms of probability density functions (pdfs). Blue and red colors show small and large probabilities, respectively. (a, b, c) Body waves differential times with respect to P- wave as a function of $t_S - t_P$. (d, e, f) SKS differential times with respect to PP- wave as a function of $t_{SS} - t_{PP}$, for events S976a and S1000a. Markers and error bars represent observed differential arrival times and their uncertainty (Table S1.1), respectively. Distributions of families A and B result from the same 3D inversion, but they are shown here separately. Among all the output models accepted by the 3D inversion, three quarters belong to Family A and one quarter to Family B.
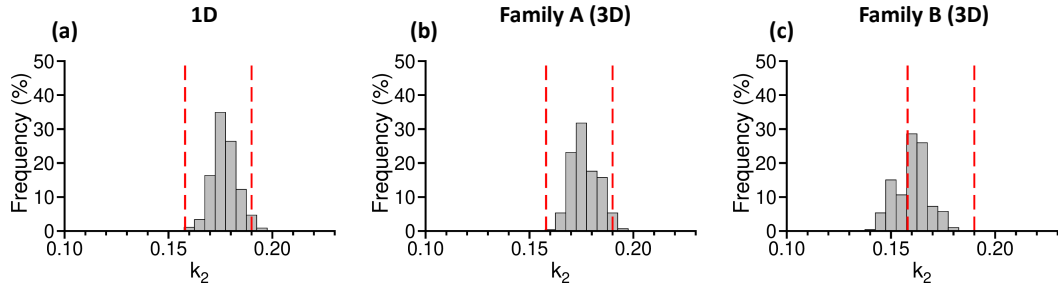
Figure S3.2. Fit of data for k_2, considering 1D models (a) and 3D Families A (b) and B (c). The red dashed lines show the 2σ uncertainty around the value of Konopliv et al. (2020) ($k_2=0.174 \quad \pm \quad 0.016$). Distributions of families A and B result from the same 3D inversion, but they are shown here separately. Among all the output models accepted by the 3D inversion, three quarters belong to Family A and one quarter to Family B.
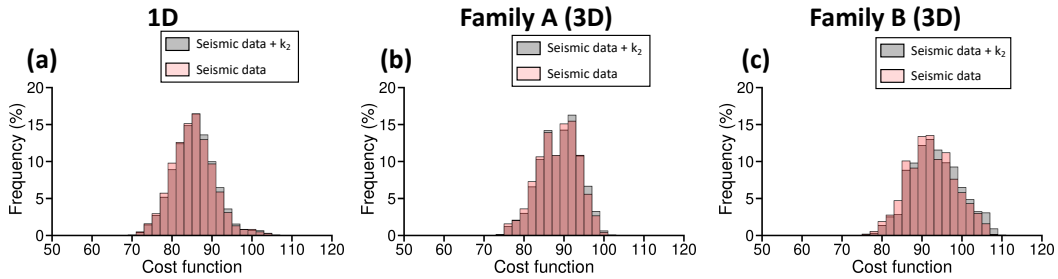
Figure S3.3. Distributions of the total cost function value as described in Equation S3.2 (in gray). The cost function calculated with seismic data only are shown in light red. Distributions of families A and B result from the same 3D inversion, but they are shown here separately. Among all the output models accepted by the 3D inversion, three quarters belong to Family A and one quarter to Family B.

S. 5 Additional inversion sets considering either seismic data, or k_2

To investigate the influence of the different geophysical observables in the inversion results, we performed additional inversion sets considering either the body wave differential times, or k_2 in the cost function (Equation S3.2). The proportion of models belonging to families A and B for each inversion run are listed in Table S5.1. We considered that the models with a potential temperature larger and smaller than 1600 K belong to Families A and B, respectively (see Figure 2c1,c2,c3).

For 1D models, when the body wave differential times and k_2 are inverted independently, the proportions of families A and B are approximately three-quarters and one-quarter. The joint inversion of the body wave differential times and k_2 considerably reduces the proportion of the Family B (only 1 %). When a 3D crust is considered, the separate inversions of the body wave differential times and k_2 result in proportions of Family B of 31 and 44 %, respectively. The joint inversion reduces the proportion of Family B to one quarter.

These results show that compared to the 1D case, the addition of the 3D crust makes it possible to retain a significant fraction of Family B models, due to the trade-offs between the velocity model, the location of the seismic events, and the travel time corrections due to the lateral crustal thickness variations.

Table S5.1.   Summary of inversion runs performed using different type of models and misfits.

Type of models	Misfit	Family A (%)	Family B (%)
1D	body waves + k_2	99	1
1D	body waves	73	27
1D	k_2	79	21
3D	body waves + k_2	77	26
3D	body waves	69	31
3D	k_2	56	44

1D models

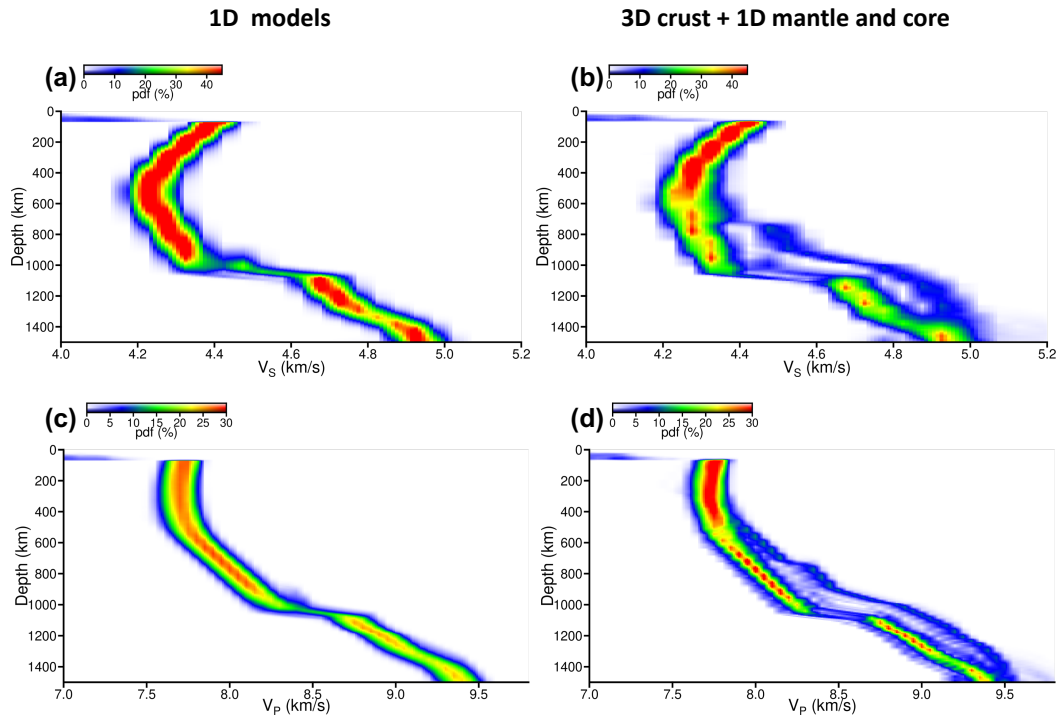**3D crust + 1D mantle and core**

Figure S4.1. Panels (a,b) and (c,d) show the *a posteriori* probability density functions (pdfs) of V_S and V_P profiles, considering the 1D models (left) and models including lateral variations of the crustal thickness (right). Blue and red colors show small and large probabilities, respectively.
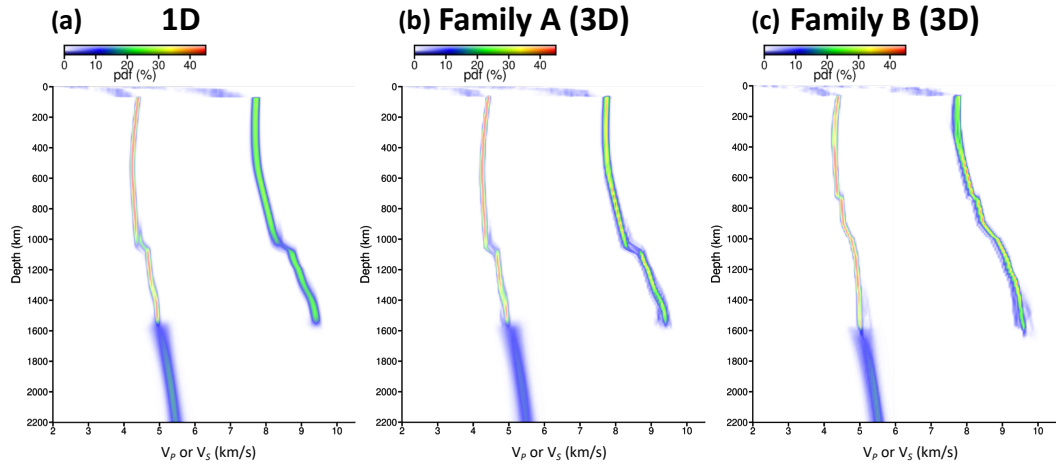

Figure S4.2. Same as Figure 1 (main text), but the results are represented as probability density functions (pdfs). Blue and red colors show small and large probabilities, respectively. Distributions of families A and B result from the same 3D inversion, but they are shown here separately. Among all the output models accepted by the 3D inversion, three quarters belong to Family A and one quarter to Family B.

S. 6 Crustal thickness distributions

The posterior distributions of the average crustal thickness of Mars, the crustal density, and the density contrast between the crust and mantle at Moho, considering 1D and 3D models, are displayed in Figure S6.1. To satisfy receiver function constraints on the crustal thickness beneath InSight (Wieczorek et al., 2022), only the models lying in the range of 30–72 km are accepted by the algorithm (Figure S6.1a-c).

The crustal thickness distribution below each epicenter location is shown in Figure S6.2. For seismic events located close to the crustal dichotomy between the Northern and the Southern hemispheres, or in the vicinity of a major geological structure, the distributions are clearly multimodal.
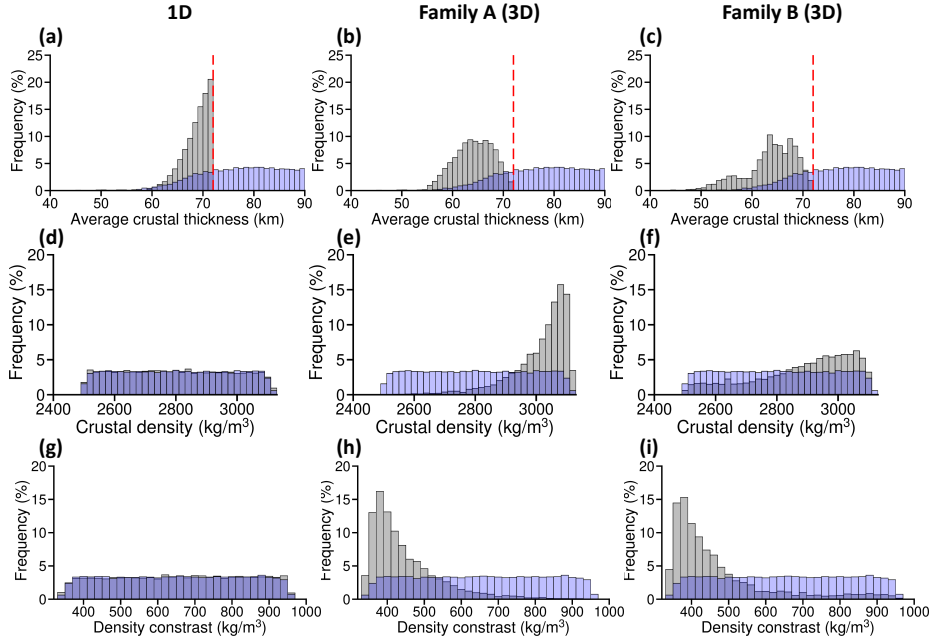

Figure S6.1. Marginal prior (in blue) and posterior (in grey) distributions of the average crustal thickness of Mars (a-c), the crustal density (d-f), and the density contrast between the crust and mantle at Moho (g-i), considering 1D models (left), 3D Family A (middle) and 3D Family B (right). The red dashed lines in panels (a-c) show the upper bound at 72 km authorized in our inversion, to satisfy receiver function constraints on the crustal thickness beneath InSight (Wieczorek et al., 2022). Distributions of families A and B result from the same 3D inversion, but they are shown here separately. Among all the output models accepted by the 3D inversion, three quarters belong to Family A and one quarter to Family B.
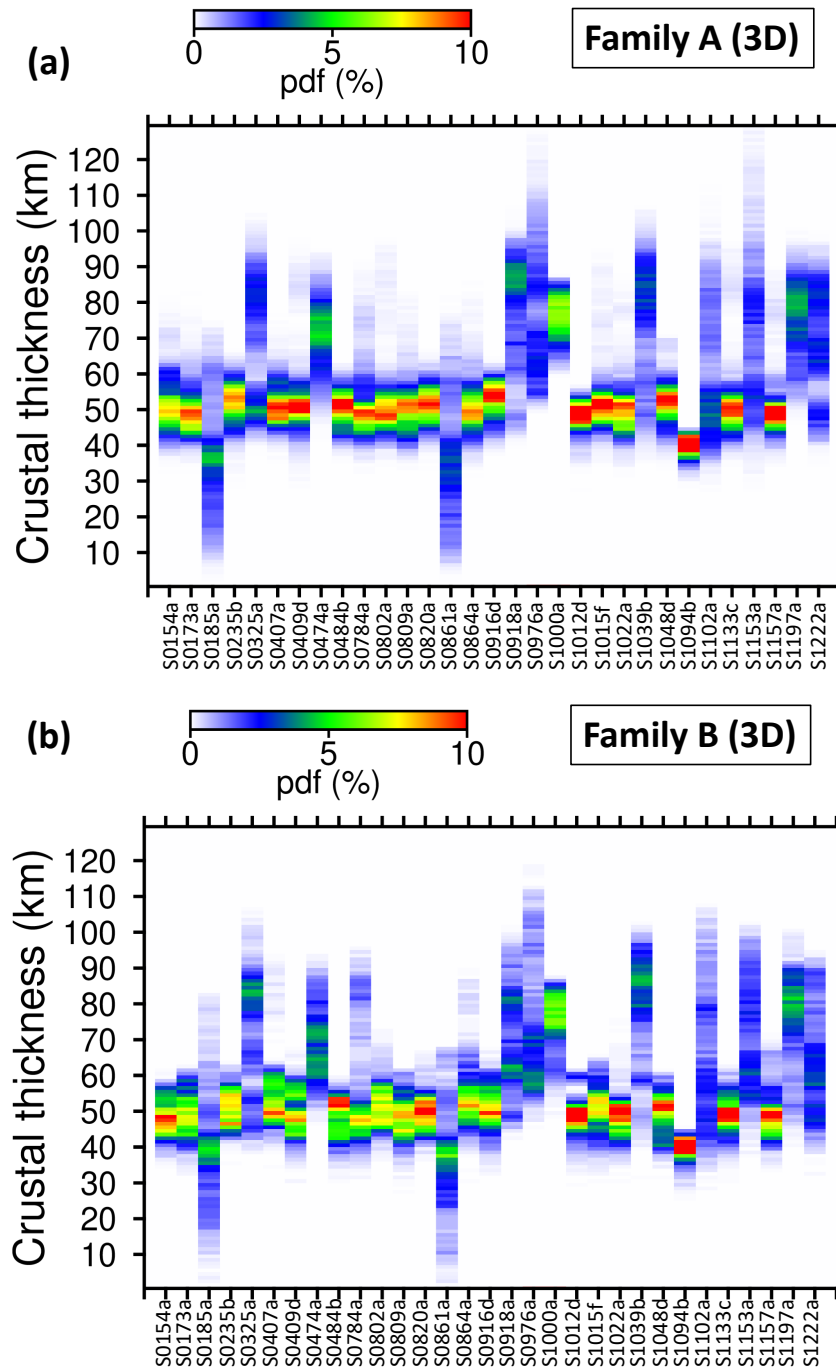
Figure S6.2. *A posteriori* probability density functions (pdfs) of the crustal thickness below each epicenter location for the 31 seismic events considered in Table S1.1. All the models accepted by the Bayesian algorithm are shown. The results for Families A and B are displayed in (a) and (b), respectively. Blue and red colors show small and large probabilities, respectively. Distributions of families A and B result from the same 3D inversion, but they are shown here separately. Among all the output models accepted by the 3D inversion, three quarters belong to Family A and one quarter to Family B.

S. 7 Marsquake locations

The mean values and uncertainties of epicentral distance, back azimuth, and depth of the 31 seismic events considered in this study, are summarized in Table S7.1 and displayed in Figure S7.1 for each set of models. The locations of the two meteorite impacts S1000a and S1094b are fixed (Posiolova et al., 2022). The latitude and longitude of the seismic events are also summarized in Table S7.1. The distances from the InSight lander are provided in kilometers in Table S7.2.

S. 8 Travel time corrections due to the 3D crust

The travel time corrections applied for each considered differential time and each seismic event are shown in Figure S8.1 and Figure S8.2 for Families A and B, respectively.

S. 9 Additional inversion sets using a relaxed prior on the average crustal thickness

To investigate the influence of the prior bounds of the average crustal thickness of Mars in the inversion results (see Section S. 2.3), we performed additional inversion sets considering that the average crustal thickness does not have to be comprised in the bounds that satisfy receiver function constraints on the crustal thickness beneath InSight (*i.e.* between 30 and 72 km, Wieczorek et al. (2022)).

The posterior distributions of the average crustal thickness of Mars for 1D and 3D models, are displayed in Figure S9.1. As already highlighted in Drilleau et al. (2022), in the absence of tight prior bounds on the average crustal thickness, a large range of possible values is retrieved, with mean values of 100^{+17}_{-14} km and 93^{+19}_{-13} km for 1D and 3D models, respectively. For 3D models, the crustal thickness at the InSight landing site is 78^{+18}_{-13} km. As explained in Section 5 of the main text, the crustal thickness is largely influenced by the bulk HPE content (Drilleau et al., 2021; Knapmeyer-Endrun et al., 2021), and thus the planet composition (here EH45). HPE favour crustal production, resulting in a significant number of models for which the average crustal thickness is larger than 72 km. In the absence of prior provided in Wieczorek et al. (2022), the crustal density and thus the density contrast between the crust and mantle at Moho are unconstrained. For the 3D models, the crustal thickness distribution below each epicenter location is shown in Figure S9.2.

Table S7.1. Summary of the seismic events' locations. For Families A and B (3D), the locations (epicentral distance, back azimuth, and depth) correspond to output of the inversion. For 1D models, only epicentral distance and depth are estimated in the inversion, and the latitude and longitude of the epicenters are computed using the back azimuth measurements in Table S1.1. Latitude and longitude values reported in this Table are those shown in Figure 3. The superscripts '★' indicate the impact events.

Event	Epicentral distance (°)			Back azimuth (°)		Depth (km)			Latitude, Longitude (°)		
	1D	Family A (3D)	Family B (3D)	Family A (3D)	Family B (3D)	Family A (3D)	Family B (3D)	1D	1D	Family A (3D)	Family B (3D)
S0154a	29.9±2.2	30.4±2.5	29.4±2.4	84.4±21.6	85.3±19.0	15.8±31.1	41.7±13.4	60.6±24.1	5.41, 165.67	6.72, 166.05	6.27, 165.11
S0173a	30.2±1.5	30.6±1.3	29.6±1.2	93.5±18.3	93.1±17.3	18.6±19.1	17.1±17.5	41.7±13.0	3.37, 165.91	2.08, 166.14	2.33, 165.23
S0185a	54.7±1.6	55.7±1.3	54.7±2.1	311.3±20.1	302.9±19.3	23.3±8.5	39.6±17.2	12.5±9.6	41.52, 90.17	36.25, 85.53	29.36, 83.94
S0235b	29.4±1.5	30.0±1.3	29.6±1.6	64.0±25.2	72.9±21.2	26.2±9.2	16.4±13.4	21.5±9.9	14.21, 163.80	16.76, 163.55	12.35, 164.50
S0325a	41.5±2.0	42.4±2.3	41.0±2.0	124.7±23.3	133.2±21.8	54.3±25.1	38.9±12.2	44.4±9.2	-19.22, 170.44	-19.19, 171.53	-23.11, 166.89
S0407a	27.9±1.6	28.3±1.7	27.9±1.1	81.3±23.1	75.3±23.0	29.5±13.7	57.2±25.2	33.7±10.1	9.17, 163.38	8.13, 163.86	10.88, 163.08
S0409d	30.3±2.2	30.3±2.0	29.5±1.6	83.4±25.3	87.9±18.7	23.7±8.9	20.2±9.0	24.0±7.2	7.95, 165.90	7.24, 165.98	4.98, 165.18
S0474a	19.7±2.5	20.3±2.1	19.5±1.7	28.9±14.8	28.8±15.1	57.6±24.1	17.6±20.8	55.9±18.7	23.00, 143.15	22.28, 146.04	21.67, 145.59
S0484b	30.8±1.8	30.9±1.5	31.2±1.6	76.9±19.5	84.4±16.8	40.6±12.7	24.7±17.5	45.0±15.6	12.60, 165.74	10.66, 166.21	6.76, 166.89
S0784a	30.6±1.8	29.4±1.9	31.1±2.5	99.8±17.2	115.6±23.7	13.5±11.2	36.1±12.5	18.7±8.4	-1.50, 165.70	-0.93, 164.59	-9.09, 163.76
S0802a	27.9±2.3	28.6±1.7	28.0±2.1	86.4±19.7	80.1±20.5	30.1±10.7	29.5±10.2	17.0±8.9	6.34, 163.63	5.69, 164.28	8.66, 163.54
S0809a	29.4±2.8	30.0±2.4	29.0±2.1	85.3±19.3	92.6±16.9	25.5±9.4	22.6±9.1	20.0±10.0	5.77, 165.14	6.28, 165.73	2.67, 164.58
S0820a	29.4±2.3	29.7±1.9	30.9±4.5	84.8±24.3	84.7±17.9	18.6±8.8	19.9±6.6	18.6±8.1	6.89, 165.04	6.48, 165.35	6.60, 166.57
S0861a	55.1±3.0	56.0±3.5	54.9±3.2	310.0±18.4	305.5±14.7	60.1±26.9	70.8±23.0	38.5±28.4	37.29, 86.89	35.30, 86.66	31.50, 84.38
S0864a	29.5±3.2	29.3±3.0	28.7±2.1	82.6±19.8	81.3±29.4	56.1±20.0	15.8±26.6	38.3±15.5	7.15, 165.20	7.56, 164.92	8.18, 164.29
S0916d	29.4±1.4	29.6±1.2	29.4±1.2	64.3±17.6	78.4±20.3	14.7±32.1	34.6±14.9	30.8±20.0	13.25, 164.08	16.48, 163.27	9.65, 164.85
S0918a	16.8±2.2	17.3±1.7	17.0±2.8	165.3±24.0	152.9±17.6	23.9±20.1	50.1±18.4	56.5±26.2	-11.60, 140.98	-12.39, 140.04	-10.76, 143.38
S0976a	143.7±2.6	144.2±3.2	144.7±5.6	77.0±20.0	77.0±21.8	68.5±29.8	37.3±40.9	52.5±29.5	1.29, -80.38	3.70, -79.22	3.60, -78.73
S1000a★	126.09	126.09	126.09	34.0	34.0	0	0	0	38.11, -79.88	38.11, -79.88	38.11, -79.88
S1012d	37.6±1.9	36.7±3.7	37.1±2.2	61.6±18.0	61.7±17.7	17.7±5.1	20.6±6.7	15.6±5.4	20.23, 170.84	20.42, 169.74	20.50, 170.17
S1015f	30.1±2.1	30.4±3.0	28.4±3.0	77.0±22.8	80.9±15.1	23.3±8.4	37.6±16.0	26.1±8.8	8.69, 165.61	10.49, 165.72	8.32, 163.94
S1022a	29.4±2.2	30.7±1.9	30.0±1.8	85.0±20.6	94.7±14.7	19.0±5.0	18.0±5.0	21.3±6.0	4.66, 165.10	6.45, 166.40	1.52, 165.49
S1039b	30.1±2.8	29.8±1.9	30.0±2.1	141.2±25.7	146.4±17.9	13.9±21.7	19.3±22.0	38.1±13.1	-18.62, 155.48	-18.82, 154.85	-20.63, 152.80
S1048d	30.8±1.7	30.4±2.7	29.4±3.1	70.3±16.8	78.8±13.4	32.5±14.3	58.3±29.9	35.1±12.1	12.09, 165.82	13.82, 164.97	9.47, 164.83
S1094b★	58.5	58.5	58.5	51.4	51.4	0	0	0	34.80, -170.08	34.80, -170.08	34.80, -170.08
S1102a	75.7±2.9	78.2±6.1	87.4±7.0	84.8±18.6	78.6±18.0	97.2±46.1	54.8±36.9	57.1±23.1	9.85, -148.15	6.04, -145.75	11.60, -136.10
S1133c	29.5±2.1	29.5±2.6	28.3±2.1	89.7±19.1	86.1±15.1	18.4±5.6	14.2±5.2	18.3±4.5	4.90, 165.26	4.08, 165.22	5.85, 164.03
S1153a	82.2±2.7	83.1±6.3	84.8±3.7	94.6±20.5	95.9±19.0	112.8±60.5	45.1±18.2	95.9±42.4	-6.38, -142.77	-4.05, -141.62	-5.55, -140.09
S1157a	36.9±2.1	36.6±3.4	36.3±4.3	91.3±20.6	91.0±20.6	37.2±14.3	39.6±13.0	30.3±7.7	5.10, 172.69	2.84, 172.29	3.00, 171.96
S1197a	32.2±2.0	32.3±2.1	32.4±1.4	242.9±18.0	246.4±14.1	29.4±10.1	33.4±10.5	35.7±10.3	-10.23, 106.8	-10.32, 106.74	-8.67, 171.98
S1222a	37.6±2.4	37.9±2.9	37.1±2.6	131.0±20.1	124.0±17.1	63.4±21.3	47.0±14.1	61.7±25.0	-16.35, 167.39	-20.14, 165.17	-16.08, 166.97

Table S7.2. Summary of the distance in kilometers between the seismic sources and the In-Sight lander. The superscripts '⋆' indicate the impact events.

| Event	1D	Family A (3D)	Family B (3D)
S0154a	1771.6±132.2	1796.7±147.1	1739.6±144.1
S0173a	1788.7±90.0	1808.1±76.7	1753.2±73.8
S0185a	3234.1±97.4	3292.0±77.5	3233.5±126.4
S0235b	1738.0±87.0	1771.8±76.6	1749.7±96.6
S0325a	2456.5±117.2	2509.6±137.1	2423.0±120.1
S0407a	1652.9±95.7	1674.1±102.8	1651.7±67.1
S0409d	1792.0±131.2	1793.0±120.1	1742.8±93.9
S0474a	1165.3±146.1	1199.1±123.6	1156.1±100.3
S0484b	1823.2±109.0	1829.1±90.9	1845.3±92.3
S0784a	1812.1±110.7	1741.6±111.6	1840.0±150.0
S0802a	1653.1±136.8	1689.8±99.1	1658.1±123.5
S0809a	1741.1±164.2	1776.1±145.0	1713.0±127.0
S0820a	1737.4±136.2	1753.7±114.2	1826.6±268.4
S0861a	3256.9±179.4	3135.8±204.5	3249.5±189.4
S0864a	1747.5±192.5	1734.5±175.9	1698.7±121.5
S0916d	1738.5±85.0	1750.9±71.0	1741.3±70.7
S0918a	992.7±128.9	1021.3±103.5	1002.7±166.8
S0976a	8493.0±151.2	8535.5±186.4	8562.0±330.9
S1000a⋆	7459.2	7459.2	7459.2
S1012d	2226.0±115.3	2176.7±210.1	2196.9±132.8
S1015f	1779.0±122.1	1799.0±175.4	1679.2±176.7
S1022a	1738.4±131.0	1815.7±115.5	1772.7±105.6
S1039b	1780.1±165.8	1765.3±112.4	1776.8±121.6
S1048d	1821.0±102.4	1797.4±158.2	1738.7±184.0
S1094b⋆	3460.7	3460.7	3460.7
S1102a	4477.6±170.8	4629.9±361.6	5171.6±416.9
S1133c	1747.6±121.7	1747.0±154.7	1675.6±121.7
S1153a	4861.2±158.5	4916.4±371.3	5014.4±220.7
S1157a	2185.4±124.8	2165.8±202.1	2147.8±255.2
S1197a	1904.4±120.8	1909.3±126.3	1917.7±85.0
S1222a	2223.3±143.3	2241.9±170.6	2194.5±154.2
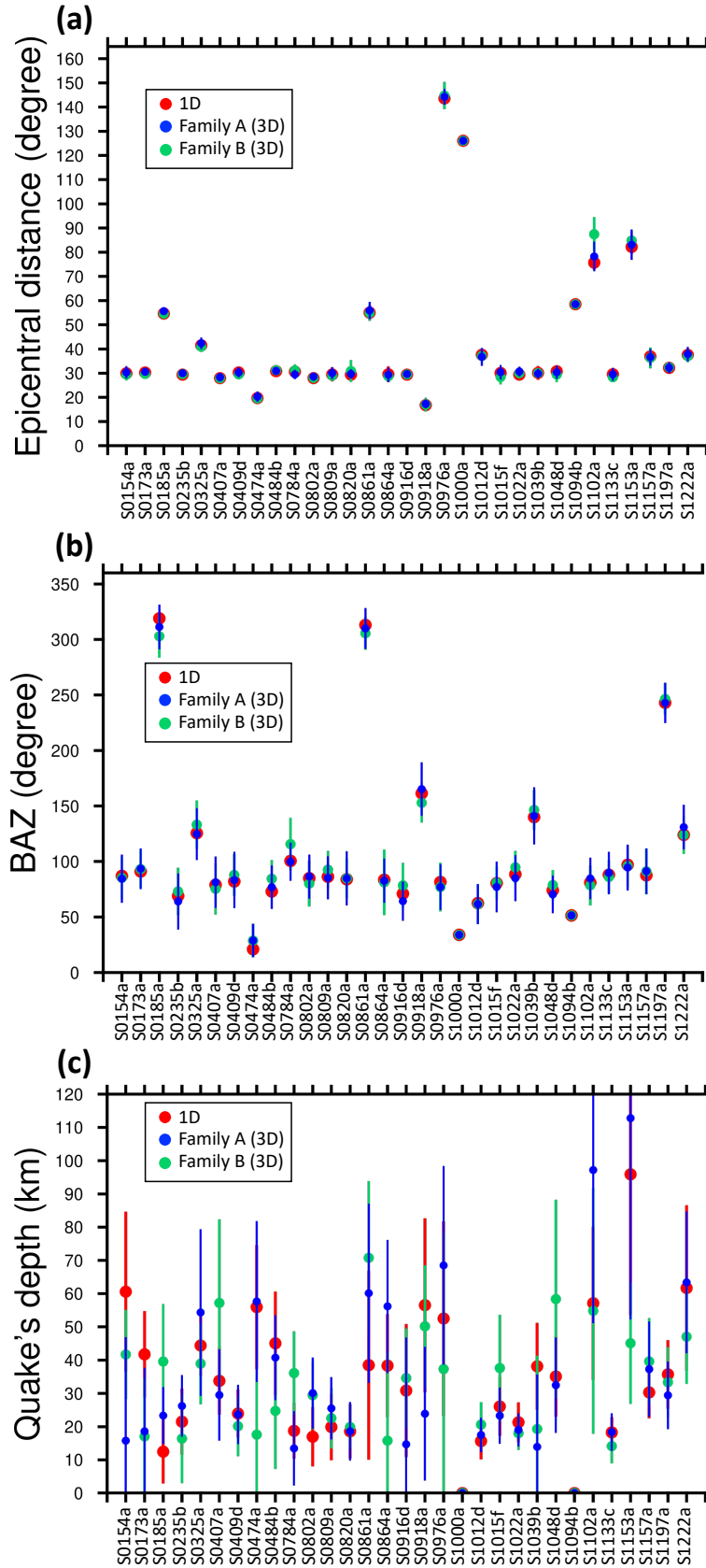
Figure S7.1. Mean values and uncertainties of the epicentral distances (a), back azimuths (b), and depths (c) of the 31 seismic events. The results considering 1D models, and Families A and B (3D), are shown in red, blue, and green, respectively.
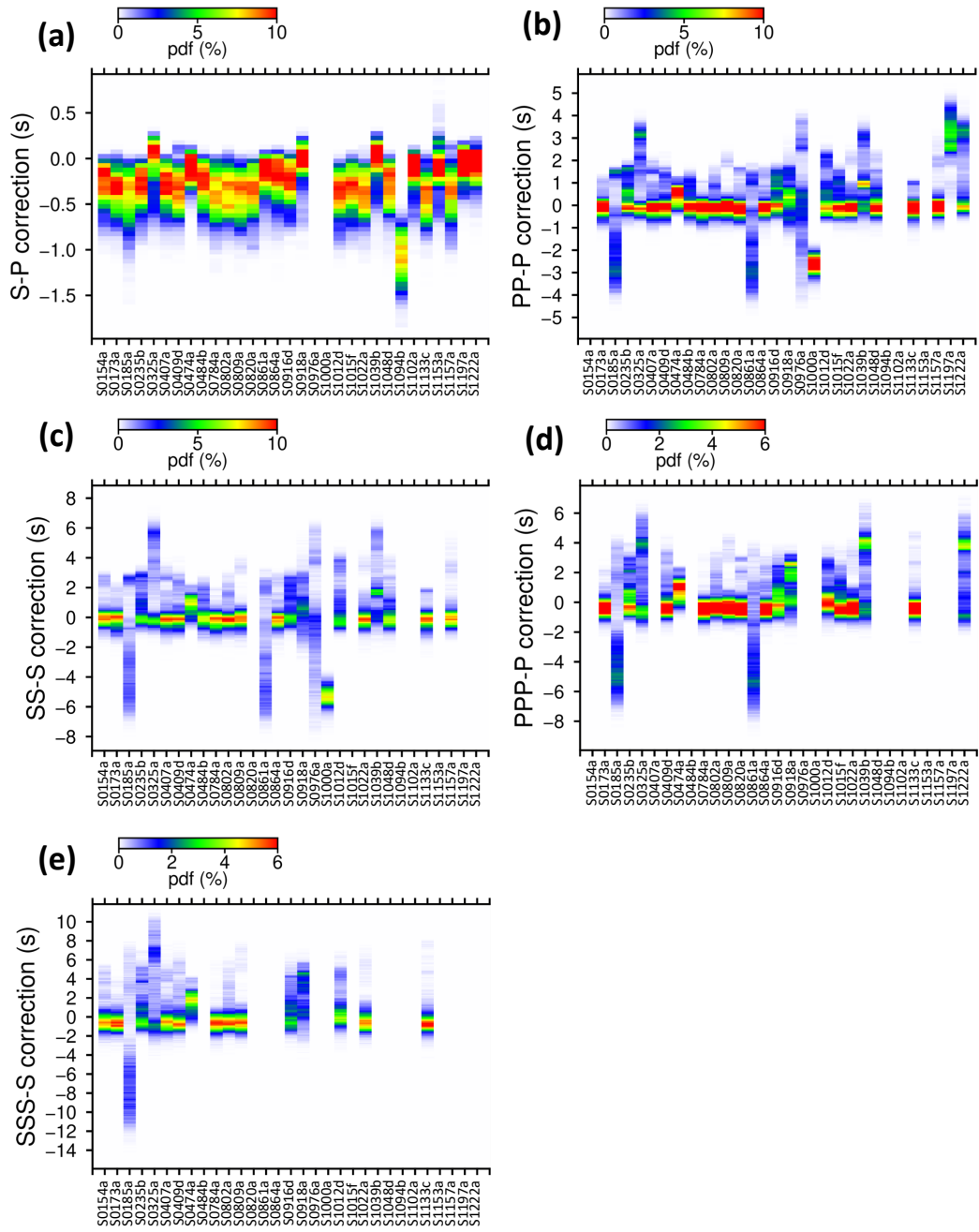
Figure S8.1. *A posteriori* probability density functions (pdfs) of the travel time corrections (in s) applied for Family A. All the models accepted by the Bayesian algorithm are shown.
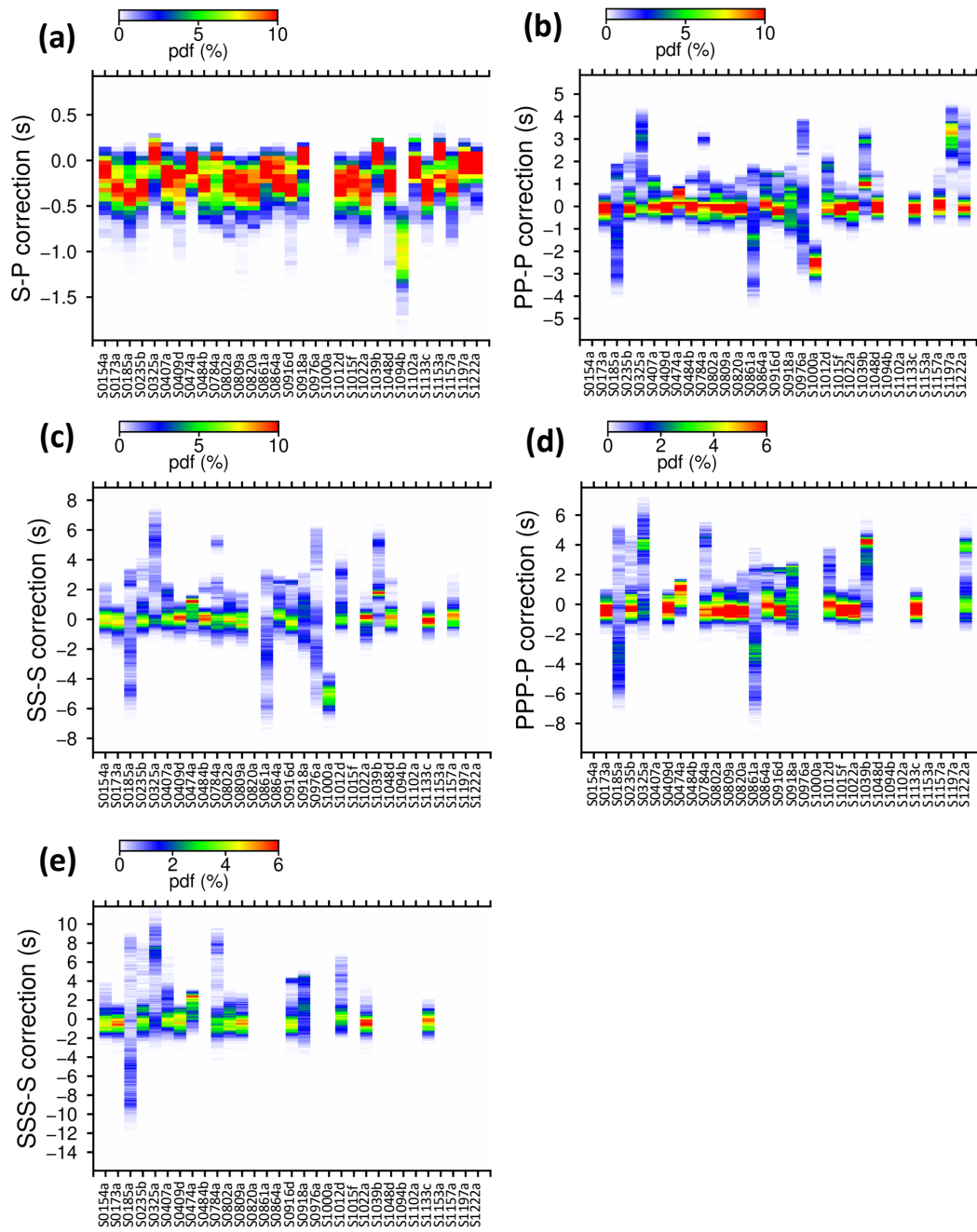
Figure S8.2. *A posteriori* probability density functions (pdfs) of the travel time corrections (in s) applied for Family B. All the models accepted by the Bayesian algorithm are shown.
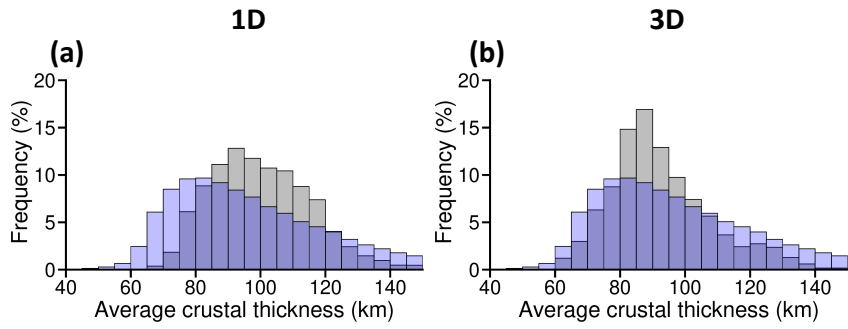
Figure S9.1. Marginal prior (in blue) and posterior (in grey) distributions of the average crustal thickness of Mars, considering 1D (a) and 3D (b) models. In these inversion sets, the average crustal thickness is not forced to be comprised in the bounds that satisfy receiver function constraints on the crustal thickness beneath InSight (Wieczorek et al., 2022).
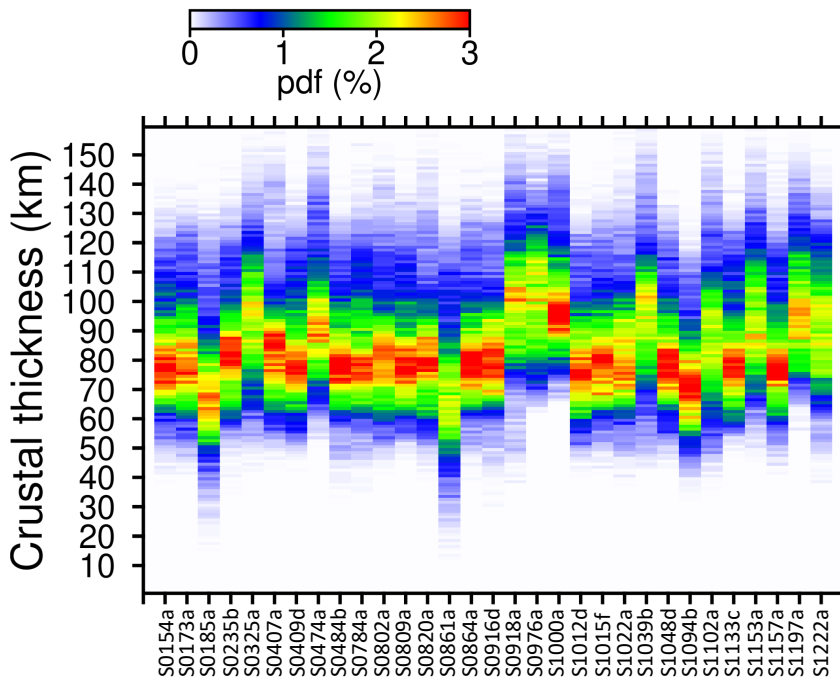

Figure S9.2. *A posteriori* probability density functions (pdfs) of the crustal thickness below each epicenter location for the 31 seismic events considered in Table S1.1. In this inversion set, the average crustal thickness is not forced to be comprised in the bounds that satisfy receiver function constraints on the crustal thickness beneath InSight (Wieczorek et al., 2022). All the models accepted by the Bayesian algorithm are shown. Blue and red colors show small and large probabilities, respectively.

References

Breuer, D., & Spohn, T. (2003). Early plate tectonics versus single-plate tectonics on Mars: Evidence from magnetic field history and crust evolution . *Journal of Geophysical Research*, *108*, doi:10.1029/2002JE001999.

Drilleau, M., Samuel, H., Garcia, R. F., Rivoldini, A., Perrin, C., Michaut, C., ... Banerdt, W. B. (2022). Marsquake locations and 1-D seismic models for Mars from InSight data. *Journal of Geophysical Research: Planets*, *127*(9). doi: 10.1029/2021JE007067

Drilleau, M., Samuel, H., Rivoldini, A., Panning, M., & Lognonné, P. (2021, 03). Bayesian inversion of the Martian structure using geodynamic constraints. *Geophysical Journal International*. doi: 10.1093/gji/ggab105

Durán, C., Khan, A., Ceylan, S., Zenhäusern, G., Stähler, S., Clinton, J., & Giardini, D. (2022). Seismology on Mars: An analysis of direct, reflected, and converted seismic body waves with implications for interior structure. *Physics of the Earth and Planetary Interiors*, 106851. doi: 10.1016/j.pepi.2022.106851

Grott, M., & Breuer, D. (2008). The evolution of the martian elastic lithosphere and implications for crustal and mantle rheology. *Icarus*, *193*(2), 503–515.

Hauck, S. A., & Phillips, R. J. (2002). Thermal and crustal evolution of Mars. *Journal of Geophysical Research*, *107*, doi:10.1029/2001JE001801.

Irving, J. C. E., Lekić, V., Duran, C., Drilleau, M., Kim, D., Rivoldini, A., ... Xu, Z. (2023). First observations of core-transiting seismic phases on Mars. *Proc. Nat. Acad. Sci.*, *120*(18), e2217090120. doi: 10.1073/pnas.221709012

Knapmeyer-Endrun, B., Panning, M. P., Bissig, F., Joshi, R., Khan, A., Kim, D., ... Banerdt, W. B. (2021). Thickness and structure of the Martian crust from InSight seismic data. *Science*, *373*(6553), 438–443. doi: 10.1126/science.abf8966

Konopliv, A. S., Park, R. S., Rivoldini, A., Baland, R. M., Le Maistre, S., Van Hoolst, T., ... Dehant, V. (2020). Detection of the Chandler Wobble of Mars From Orbiting Spacecraft. *Geophysical Research Letters*, *47*(21), 1–9. doi: 10.1029/2020GL090568

Metropolis, N., Rosenbluth, A. W., Rosenbluth, M. N., Teller, A. H., & Teller, E. (1953). Equation of state calculations by fast computing machines. *J. Chem. Phys.*, *21*, 1087–1091.

Morschhauser, A., Grott, M., & Breuer, D. (2011). Crustal recycling, mantle dehydration, and the thermal evolution of Mars. , *212*(2), 541–558.

Mosegaard, K., & Tarantola, A. (1995). Monte-Carlo sampling of solutions to inverse problems. *J. Geophys. Res.*, *100*, 12431–12447.

Posiolova, L. V., Lognonné, P., Banerdt, W. B., Clinton, J., Collins, G. S., Kawamura, T., ... Zenhäusern, G. (2022). Largest recent impact craters on Mars: Orbital imaging and surface seismic co-investigation. *Science*, *378*(6618), 412-417. doi: 10.1126/science.abq7704

Samuel, H., Drilleau, M., Rivoldini, A., Xu, Z., Huang, Q., Garcia, R. F., ... Banerdt, W. B. (2023). Geophysical evidence for an enriched molten silicate layer above Mars's core. *Nature*, *622*, 712–717. doi: 10.1038/s41586-023-06601-8

Samuel, H., Lognonné, P. H., Panning, M., & Lainey, V. (2019). The rheology and thermal history of Mars revealed by the orbital evolution of Phobos. *Nature*, *569*, 523–527. doi: 10.1038/s41586-019-1202-7

Stähler, S. C., Khan, A., Banerdt, W. B., Lognonné, P., Giardini, D., Ceylan, S., ... Smrekar, S. E. (2021). Seismic detection of the martian core. *Science*, *373*(6553), 443–448. doi: 10.1126/science.abi7730

Tarantola, A. (2005). *Inverse problem theory - and methods for model parameter estimation.* SIAM.

Thiriet, M., Breuer, D., Michaut, C., & Plesa, A.-C. (2018). Scaling laws of convection for cooling planets in a stagnant lid regime. *Physics of the Earth and Plane-*

tary Interiors, *286*, 138–153. doi: 10.1016/j.pepi.2018.11.003

Tosi, N., Godolt, M., Stracke, B., Ruedas, T., Grenfell, J. L., Höning, D., . . . Spohn, T. (2017). The habitability of a stagnant-lid Earth. *Astronomy and Astrophysics*, *605*, doi:10.1051/0004-6361/201730728.

Wieczorek, M. A., Broquet, A., McLennan, S. M., Rivoldini, A., Golombek, M., Antonangeli, D., . . . Banerdt, W. B. (2022). Insight constraints on the global character of the Martian crust. *Journal of Geophysical Research: Planets*, *127*(5). doi: 10.1029/2022JE007298